fibers

MDPI

Article

Bacterial Cellulose-Containing Alginate Inks: A Proof-of-Concept Study on Acellular 3D Printing Feasibility and Cytocompatibility

Elena Utoiu [1], Elena Iulia Oprita [1,*], Vasile-Sorin Manoiu [1], Rodica Tatia [1], Claudiu Utoiu [2], Doriana Nicoleta Banu [3], Mihai Raduca [3] and Oana Craciunescu [1]

[1] National Institute of Research and Development for Biological Sciences, 060031 Bucharest, Romania; elena.utoiu@incdsb.ro (E.U.); sorin.manoiu@incdsb.ro (V.-S.M.); rodica.tatia@incdsb.ro (R.T.); oana.craciunescu@incdsb.ro (O.C.)

[2] National Research and Development Institute for Food Bioresources—IBA, 020323 Bucharest, Romania; claudiu.utoiu@bioresurse.ro

[3] "Costin D. Nenițescu" Institute of Organic and Supramolecular Chemistry of the Romanian Academy, 060023 Bucharest, Romania; doriana.banu@icoscdn.ro (D.N.B.); mihai.raduca@icoscdn.ro (M.R.)

* Correspondence: iulia.oprita@incdsb.ro

Abstract

The development of hydrogel bioinks that combine structural stability with biological compatibility remains a major challenge in extrusion-based 3D printing for tissue engineering. In this proof-of-concept study, bacterial cellulose (BC) obtained from kombucha fermentation was explored as a sustainable nanofibrillar component for alginate/chondroitin sulfate (CS)/silicon-substituted hydroxyapatite (Si-HA) composite inks. Following alkaline purification, mechanical processing, and freeze-drying, BC was characterized by scanning electron microscopy (SEM), ATR-FTIR spectroscopy, and X-ray diffraction (XRD), revealing a highly entangled nanofibrillar architecture with high crystallinity (85.4%) and strong hydrogen-bonding potential. Four hydrogel formulations were developed as a comparative 2 × 2 matrix, contrasting BC-containing systems with methylcellulose (MC)-containing reference systems at two Si-HA loadings. Reduced-viscosity measurements of the uncrosslinked precursor formulations showed higher values at the lower Si-HA loading in both formulation series. All formulations could be extruded as acellular inks into grid-like constructs and retained identifiable macroporous architectures after ionic crosslinking. Swelling increased between 24 and 48 h, while mass loss remained limited after the initial 24 h incubation period. In direct-contact testing with L929 fibroblasts, cell viability remained above 84% after 48 h, meeting the ISO 10993-5 non-cytotoxicity criterion. These findings support the feasibility of incorporating physically processed kombucha-derived BC into alginate-based composite inks.

Keywords: bacterial cellulose; extrusion-based 3D printing; hydrogel ink; tissue engineering; alginate; chondroitin sulfate; biomaterials

Check for updates

Received: 30 June 2026
Revised: 15 August 2026
Accepted: 21 August 2026
Published: 25 August 2026

Copyright: © 2026 by the authors. Licensee MDPI, Basel, Switzerland. This article is an open access article distributed under the terms and conditions of the Creative Commons Attribution (CC BY) license.

1. Introduction

The field of tissue engineering has experienced a profound paradigm shift with the advent of extrusion-based 3D printing, a technology that allows the construction of customized, biomimetic architectural scaffolds with high precision [1,2]. To replicate the native extracellular matrix (ECM), a hydrogel bioink formulation must strike a delicate balance between providing biological signaling and maintaining structure over time [1–3].

Hydrophilic polysaccharides, such as alginate and chondroitin sulfate (CS), are natural choices for foundational biomaterial ink matrices due to their structural similarity to ECM constituents and good biocompatibility [2,4,5]. However, these soft networks are fragile; they frequently suffer from poor mechanical stability, low shape fidelity during the extrusion process, and rapid degradation post-printing, which limit their applicability in load-bearing or long-term tissue engineering constructs [1,3,6].

A promising approach to overcome these limitations is the incorporation of nanofibrous reinforcing phases that can act as structural anchors within the hydrogel matrix. In this context, bacterial cellulose (BC) has gained increasing attention as a suitable component for advanced composite bioinks [7,8]. Unlike plant-derived cellulose, microbial BC forms an ultrafine, highly pure three-dimensional network of crystalline nanofibrils with a high length-to-diameter ratio (high aspect ratio), contributing to mechanical reinforcement and high water-retention capacity in cellulose-containing composites [9,10]. These structural features allow BC to mimic several characteristics of the collagen-rich extracellular matrix (ECM), thereby supporting favorable cell–material interactions and improved scaffold stability [7,11]. From a sustainability perspective, BC can also be recovered from kombucha fermentation byproducts, supporting circular bioeconomy principles through waste valorization and low-cost biopolymer production [7,12]. Although BC has demonstrated considerable potential for hydrogel and scaffold development, relatively few studies have investigated the direct incorporation of physically processed kombucha-derived BC into complex polyanionic bioink systems without prior chemical functionalization or surface modification [8,13].

However, transforming raw bacterial cellulose membranes into a reliable and printable biomaterial formulation remains challenging. Achieving an optimal rheological profile—sufficiently fluid to enable smooth extrusion while viscous enough to maintain filament shape after deposition—continues to be a persistent challenge in bioink development [1,14,15]. Most existing approaches improve BC dispersion and printability through chemical modifications such as TEMPO oxidation, maleic acid grafting, or charge modification [13,16–18]. Although these strategies often enhance processing performance, they can also increase formulation complexity, leave residual chemical reagents, and potentially compromise cytocompatibility. By contrast, physical processing methods based on alkaline purification, mechanical grinding, and lyophilization remain relatively underexplored. Nevertheless, these processing steps play a critical role in defining fiber morphology, rehydration capacity, and interfacial interactions within the polymer network, ultimately influencing scaffold swelling behavior and degradation kinetics under physiological conditions [9,17,19].

To further enhance scaffold functionality beyond BC-mediated nanostructural reinforcement, the incorporation of inorganic bioactive phases represents a promising strategy. Silicon-substituted bioceramics, particularly silicon-substituted hydroxyapatite (Si-HA), have attracted considerable attention due to their ability to release biologically relevant calcium and silicon ions, which are known to stimulate cell proliferation, differentiation, and extracellular matrix synthesis [20–22].

The aim of this proof-of-concept study was to assess whether physically processed kombucha-derived BC, used without chemical functionalization, can be incorporated into pre-crosslinked alginate/CS/Si-HA composite inks while maintaining extrusion feasibility and cytocompatibility. A 2 × 2 screening design was used to compare BC- and methylcellulose (MC)-based formulations at two Si-HA loadings. BC was characterized by SEM, ATR-FTIR, and XRD, while the resulting formulations were evaluated in terms of intrinsic viscosity, swelling, mass loss in phosphate-buffered saline (PBS), qualitative extrusion-printing feasibility, and direct-contact cytocompatibility with L929 fibroblasts. The working

hypothesis was that the nanofibrillar and highly crystalline structure of BC would allow its incorporation as a structural cellulose component within the alginate-based matrix without preventing extrusion or compromising short-term cytocompatibility. As an exploratory study, the work was not intended to demonstrate mechanical superiority, quantitative validation of printing fidelity, or tissue-specific performance.

2. Materials and Methods

2.1. Materials

Si-substituted hydroxyapatite (Si-HA) was kindly provided by SC CHEMI CERAMIC F SRL, Sf Gheorghe, Romania. Sodium alginate (180947), chondroitin sulfate (CS) from bovine trachea (C9819), methyl cellulose (MC) with a viscosity of 1500 cP (M0387), sodium hydroxide, high-density polyethylene (HDPE) granules and phenol were purchased from Sigma-Aldrich (Hamburg, Germany). NCTC clone 929 cell line of murine fibroblasts was acquired from the European Collection of Authenticated Cell Cultures (ECACC, Wiltshire, UK).

2.2. Preparation of Bacterial Cellulose Particles

Bacterial cellulose (BC) was purified from raw cellulosic pellicles that are naturally developed at the air–liquid interface of a sweetened black tea broth, synthesized by a symbiotic culture of bacteria and yeast (SCOBY), in a fermentation of kombucha beverages, following the preparation protocol described in our previous work [23]. A single batch of kombucha-derived bacterial cellulose was purified and used for all subsequent characterization and hydrogel formulation experiments in this proof-of-concept study. The raw pellicles were boiled in a 0.1 M NaOH solution for 1 h under continuous agitation. Following this alkaline treatment, the purified membranes were repeatedly washed with deionized water until a neutral pH was achieved [24]. The purified BC membranes were minced and processed into a particle suspension using a homogenizer. For morphological evaluation, a small amount of this wet-ground suspension was dispersed onto stubs, dried at 25 °C, and subsequently examined using a Hitachi SU-1510 scanning electron microscope (SEM) (Hitachi High-Technologies Corporation, Tokyo, Japan) operated at 15 kV accelerating voltage, to observe the particle morphology. ImageJ software (version 1.54g) was used to observe the particle morphology. To ensure precise gravimetric dosing, the BC suspension was frozen, freeze-dried, and subsequently ground into a fine powder.

2.3. Structural Characterization of BC and MC

The chemical structure and characteristic functional groups of the isolated bacterial cellulose (BC), relative to methylcellulose (MC) were investigated using FTIR-ATR spectroscopy to emphasize the native structural integrity of the microbial polymer. Spectra of the solid materials were recorded using a Bruker VERTEX 70 instrument (Billerica, MA, USA) equipped with a Harrick MVP2 diamond ATR accessory (Pleasantville, NY, USA) over the range 400–4000 cm^{-1}. Spectra were acquired at a resolution of 4 cm^{-1} using 32 scans. All data were normalized to an intensity of 2. For visual context, the spectra are displayed down to 450 cm^{-1}, as the structural interpretation used in this study is based on the characteristic cellulose and methylcellulose bands located above this wavenumber. The region below 450 cm^{-1} did not contribute additional bands relevant to the comparison performed here.

The crystalline structure and macromolecular organization of BC and MC were investigated by X-ray diffraction (XRD) before their incorporation into the hydrogel formulations in order to compare their crystallographic organization. XRD measurements were performed on a Proto AXRD Benchtop instrument (Oldcastle, Ontario, Canada) using Cu Kα

radiation (λ = 1.54059 Å). Data were collected over a 2θ range of 5–70°, with a step size of 0.02° and an exposure time of 2 s per step. All data were normalized to an intensity of 1.

Crystallite size was estimated using the Scherrer equation only for defined crystalline reflections of BC. No Scherrer analysis was applied to MC because its diffraction pattern was dominated by broad amorphous scattering.

2.4. Preparation of Composite Hydrogel Inks

Four composite hydrogel formulations were prepared using sodium alginate as the carrier matrix at a final concentration of 8% (*w*/*v*). Either bacterial cellulose (BC) or methylcellulose (MC) was incorporated together with chondroitin sulfate (CS) and Si-HA. The formulations differed according to the cellulose component and Si-HA loading, as summarized in Table 1.

Table 1. Composition and component ratios of the hydrogel ink formulations used in this study.

Formulation	Abbrev.	Composition	Ratio (*w*/*w*)	Final Concentrations (mg/mL)
Formulation 1	F1	MC:CS:Si-HA	2:1:1	MC 2; CS 1; Si-HA 1
Formulation 2	F2	MC:CS:Si-HA	2:1:0.5	MC 2; CS 1; Si-HA 0.5
Formulation 3	F3	BC:CS:Si-HA	2:1:1	BC 2; CS 1; Si-HA 1
Formulation 4	F4	BC:CS:Si-HA	2:1:0.5	BC 2; CS 1; Si-HA 0.5

All formulations contained sodium alginate at a final concentration of 80 mg/mL (8% *w*/*v*).

All constituents were homogenized under continuous magnetic stirring at 40 °C and 100 rpm for 2 h. Before $CaCl_2$ addition, aliquots of the uncrosslinked precursor formulations were collected for capillary-viscosity measurements, as described in Section 2.4.1. The remaining formulations were subsequently pre-crosslinked with 0.025 M $CaCl_2$ and degassed by centrifugation at 5000× *g* for 10 min at room temperature.

2.4.1. Determination of Hydrogel Ink Reduced Viscosity

The reduced viscosity (dL/g) of the uncrosslinked precursor formulations was determined by testing dilute solutions in distilled water at 37 °C, at a fixed concentration. All measurements were performed before the addition of $CaCl_2$. An Ubbelohde capillary viscometer housed within a VB 1423 thermostated water bath (Selecta, Madrid, Spain) was used. Reduced viscosity was calculated according to:

$$\eta_{red} = \frac{(\eta_{rel} - 1)}{C}$$

where η_{rel} is the relative viscosity and c is the concentration of the diluted formulation expressed in g/dL (we used a fixed concentration of 0.008 g/dL). Each ink formulation was analyzed in quadruplicate, and the final values were reported as the mean of the four determinations ± standard deviation (SD).

2.4.2. Determination of Swelling Degree

The swelling capacity of the isolated bacterial cellulose (BC) and crosslinked hydrogel inks was evaluated gravimetrically in accordance with established protocols [25]. Dried samples were initially weighed to determine their dry mass (Wi) and then immersed in ultrapure water at room temperature. Swelling was determined after 24 h and 48 h of incubation. At each timepoint, the samples were removed from the liquid, gently blotted with filter paper to remove excess surface water, and immediately weighed to determine the wet mass (Wf). Independent replicate samples were used for the 24 h

and 48 h measurements. The swelling degree was calculated as the percentage of water absorption relative to the initial dry weight according to the following equation:

$$Degree\ of\ swelling\ (\%) = \frac{\left(W_f - W_i\right)}{W_i} \times 100$$

2.4.3. In Vitro Stability and Mass-Loss Analysis

To evaluate the structural stability of the four crosslinked composite hydrogel formulations under simulated physiological conditions, a gravimetric mass-loss assay was performed [26]. Dry scaffold samples of a known initial weight (Wi) were submerged in 1×PBS (pH 7.4) and incubated at 37 °C for 1 to 9 days. The selected timepoints were intended to provide a preliminary assessment of early mass loss and subsequent short-term stability rather than a detailed kinetic description of degradation. At designated time intervals, the corresponding samples were retrieved, dried to a constant weight, and reweighed to determine their final dry mass (Wf). The weight loss percentage, was calculated according to the following equation:

$$Weight\ loss\ (\%) = \frac{\left(W_i - W_f\right)}{W_i} \times 100$$

2.5. Acellular Extrusion-Based 3D Printing

Preliminary printing feasibility was assessed using acellular extrusion-based 3D printing. No cells were incorporated into the hydrogel inks before or during the printing process. Printing was performed via a layer-by-layer extrusion technique using a Bio X 3D printer (Cellink, Brighton, UK) equipped with 3 mL cartridges and 25 G (0.25 mm internal diameter) metal nozzles. Porous, grid-like scaffolds (10 × 10 × 0.5 mm with 16 internal grids) consisting of two layers, were fabricated from the 4 hydrogel formulation bioinks. The printing speed was set to 1.5 mm/s for Formulations 1 and 2, and 1.6 mm/s for Formulations 3 and 4, utilizing an extrusion pressure range of 105–120 kPa, while the print bed and printing head were maintained at room temperature (≈25 °C). Immediately post-printing, the constructs were immersed in a 2% (w/v) $CaCl_2$ solution for 2 h at room temperature to complete the ionic gelation of the alginate matrix. The crosslinked scaffolds were then washed ten times with ultrapure water to thoroughly remove unreacted calcium residues. For sterilization, the scaffolds were exposed to UV light for 4 h per side within a dedicated sterile chamber (Scie-Plas, Cambridge, UK), prior to direct-contact cytocompatibility testing.

2.6. In Vitro Cytocompatibility Testing

Following acellular printing and crosslinking, the cytocompatibility of the printed constructs was evaluated separately using the direct-contact method with L929 fibroblasts, in accordance with SR EN ISO 10993-5:2009 [27]. The cells were cultured in Minimum Essential Medium (MEM) supplemented with 10% Fetal Bovine Serum (FBS), and 1% penicillin–streptomycin–neomycin. The cell culture was grown as an adherent monolayer at 37 °C in a humidified incubator with 5% CO2, to reach 85–90% confluence. For experiments, the confluent NCTC cell line was trypsinized, and the cells were seeded in 12-well culture plates at a density of 4×10^6 cells/mL. The plates were incubated for 24 h, under standard conditions of 37 °C, 5% CO_2, humidified atmosphere. After 24 h of cell attachment, the culture medium was replaced with fresh medium and the sterilized printed constructs were placed directly into the wells in contact with the cell monolayer. Untreated cells served as control. Cells treated with HDPE granules served as negative control, while 0.3% phenol solution served as positive control. The well plates were incubated under standard

conditions for 24 and 48 h. At each exposure time, the printed hydrogel constructs were carefully removed from the wells before performing the MTT assay. The assay was then carried out on the adherent L929 cells remaining in the wells, as previously described [28]. Following incubation with MTT reagent, the resulting intracellular formazan crystals were solubilized using isopropyl alcohol. The optical density of the resulting solutions was measured at 570 nm using a Spectro Star BMG spectrophotometer (Labtech, Ortenberg, Germany). The values (A_{sample} and $A_{cell\ control}$) were directly proportional to the number of viable cells in the tested culture. Cell viability is calculated using the following equation:

$$\%\ Cell\ viability\ = \frac{A_{sample}}{A_{cell\ control}} \times 100$$

The results were reported as mean ± SD from triplicate experiments.

2.7. Scanning Electron Microscopy (SEM)

For structural assessment of 3D-printed hydrogel inks and cell adhesion assessment, a scanning electron microscope (SEM) Hitachi SU-1510 (Tokyo, Japan) was used. Samples were processed in serial ethanol concentrations (12.5% to 100%) for dehydration, subsequently mounted onto aluminum stubs and sputter-coated with a thin gold layer, to provide the necessary electrical conductivity for high-resolution imaging of the scaffold's fibrillar matrix [29].

2.8. Statistical Analysis

All experiments were performed in triplicate (n = 3). The results are expressed as mean ± standard deviation (SD). The statistical analysis was carried out using one-way analysis of variance (ANOVA) and Student's t-test for pairwise comparisons between the control and treated samples. The differences were considered statistically significant at $p < 0.05$.

3. Results

3.1. Kombucha Membrane Purification

Bacterial cellulose purification from raw cellulosic pellicles synthesized by a symbiotic culture of bacteria and yeast (SCOBY) started from 146 g initial weight and reached 107 g after neutralization. These values represent the mass change observed for this individual purification batch and are not averages from replicate purification runs. To evaluate the nanofibrillar morphology, the purified BC suspension was examined using SEM, operated at an accelerating voltage of 15 kV. It observed an intricate, highly entangled network of continuous nanofibers (Figure 1).

By tracing individual fiber segments through ImageJ software, a well-distributed nanofiber diameter was observed, averaging 86 nm, spanning a tight 59 nm to 102 nm range. The micrographs are free of intact bacterial cells or organic residues, visually validating the efficacy of the alkaline purification protocol. This interconnected nanoscale morphology provides a large interfacial area that may favor physical interactions between BC fibrils and the surrounding alginate/CS matrix [30,31].

3.2. FTIR Analysis

The ATR-FTIR spectra of BC and MC are given in Figure 2. ATR-FTIR spectra confirmed the characteristic polysaccharide structure of both bacterial cellulose (BC) and me-thyl cellulose (MC) and the assignment of major bands is presented in Table 2.

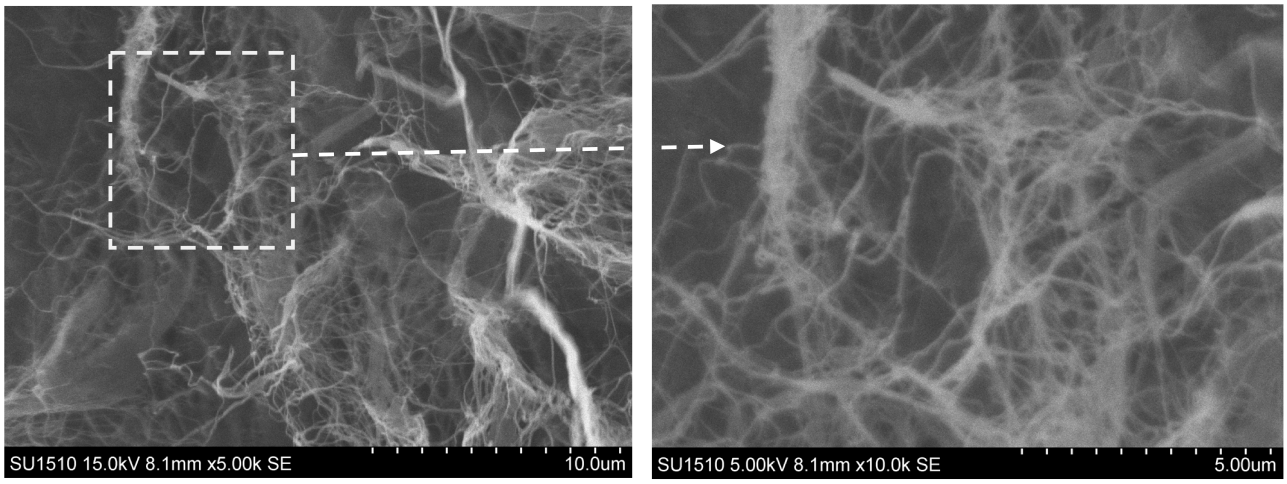


Figure 1. SEM micrographs of purified kombucha-derived bacterial cellulose showing a highly entangled nanofibrillar network at lower magnification (**A**) and a higher magnification view of the highlighted region (**B**).

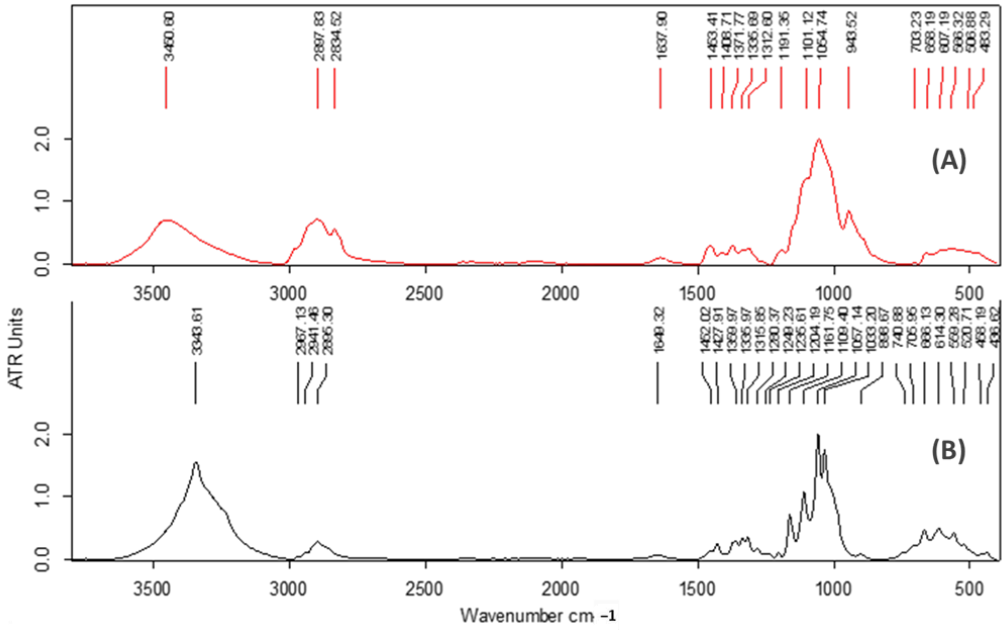


Figure 2. Side-by-side ATR-FTIR spectra comparison of bacterial cellulose (BC) (**B**) and methyl cellulose (MC) (**A**), displayed over the 4000–450 cm^{-1} region used for structural interpretation and highlighting the main differences in functional-group distribution.

Table 2. FTIR assignment of major bands [32].

Wavenumber (cm^{-1})	BC Assignment	MC Assignment
3344–3450	O-H stretching	O-H stretching
2967–2895	C-H stretching	C-H stretching
1649–1638	Bound water/carboxyl	Bound water/carboxyl
1162–1033	C-O-C/C-OH cellulose backbone	1101–1054 cm^{-1} cellulose backbone
899	β-(1→4) linkage	-
943	-	Ether linkage from methylation

ATR-FTIR spectra confirmed the characteristic polysaccharide structure of both bacterial cellulose (BC) and methyl cellulose (MC). BC exhibited a broad O–H stretching band at 3344 cm^{-1}, attributed to extensive inter- and intramolecular hydrogen bonding [33]. Peaks at 2967–2895 cm^{-1} correspond to C–H stretching vibrations [32,33]. The absorption at 1649 cm^{-1} is assigned to absorbed water and carboxyl-containing groups [32,33]. Strong bands between 1162 and 1033 cm^{-1} are characteristic of C–O–C and C–OH vibrations of the β-1,4-glucan backbone [33,34]. The signal at 899 cm^{-1} confirms β-(1→4)-glycosidic linkages [34]. MC displayed similar cellulose-derived bands, with O–H stretching at 3451 cm^{-1} and C–H stretching at 2898–2835 cm^{-1} [34], but displayed modifications associated with methyl ether substitution, including the 943 cm^{-1} band [35]. The stronger hydrogen-bonding network observed in BC indicates higher intermolecular cohesion and greater water-retention capacity (Figure 2).

The FTIR results demonstrate preservation of the cellulose backbone in both materials while highlighting the higher hydroxyl availability and hydrogen-bonding capacity of BC. These characteristics are particularly important for hydrogel formation, water retention and cellular interactions in bioink systems.

3.3. XRD Analysis

XRD analysis was performed on BC and MC as individual cellulose components before formulation. XRD patterns demonstrated major differences in supramolecular organization. BC displayed crystalline cellulose-I reflections associated with ordered nanofibrillar domains. MC exhibited a broad amorphous halo due to disruption of crystal packing by methoxy groups. The higher crystallinity of BC indicates a more ordered cellulose-I structure than that observed for MC. The possible contribution of this structural organization to the mechanical properties of the composite inks was not assessed in the present study.

X-ray diffraction patterns revealed clear differences in supramolecular organization between BC and MC. BC exhibited defined cellulose-I-associated reflections, particularly at $2\theta \approx 14.65°$ and 22.85°, consistent with ordered crystalline domains (Table 3). In contrast, the MC pattern was dominated by broad scattering features, with maxima near 8.71° and 19.85°, characteristic of a predominantly amorphous organization (Figure 3). These MC maxima were therefore treated as broad scattering features rather than as reflections from defined crystallographic planes.

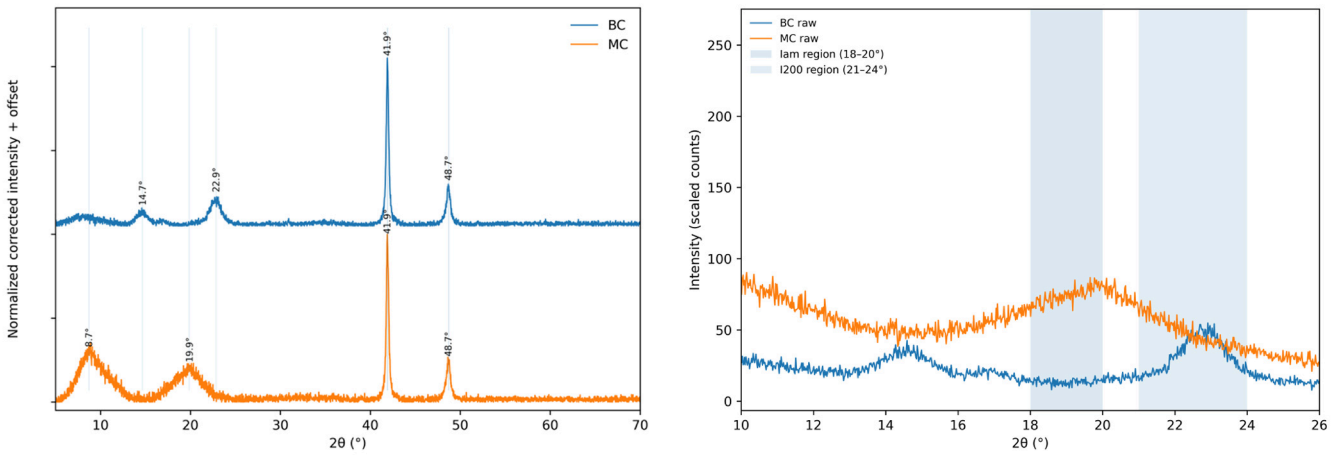
Table 3. Main XRD features and crystallinity parameters of BC and MC.

Sample	Segal CI (%)	Main XRD Features, $2\theta_2$ (°)	d-Spacing (Å)	D Scherrer (nm) *
BC	85.388	14.653, 22.853	6.040, 3.888	5.134
MC	15.901 *	broad maxima at 8.71 and 19.85	—	—

* For MC, the reported value represents an apparent Segal-type index and should not be interpreted as a true cellulose-I crystallinity index because the diffraction pattern is dominated by broad amorphous scattering.

Reflections observed at 41.91° and 48.71° were not included in the cellulose-I crystallinity assessment because they fall outside the conventional crystalline and amorphous regions used for the Segal crystallinity index. Since no blank-holder scan was available, no specific origin was assigned to these high-angle reflections.

Scherrer crystallite size was calculated only for BC crystalline reflections; no crystallite-size value was assigned to MC due to its predominantly amorphous diffraction pattern.



(**a**) (**b**)

Figure 3. Baseline-corrected diffractograms with detected peaks. (**a**) BC shows defined cellulose-I-associated reflections in the 14–23° region, whereas MC is dominated by broad scattering maxima within the 8–22° region, consistent with a predominantly amorphous structure. High-angle reflections at 41.9° and 48.7° are shown but were not used in the Segal crystallinity calculation. (**b**) Conventional Segal regions for cellulose-I crystallinity estimation: I_{am} region (18–20°) and I_{200} region (21–24°).

PXRD analysis demonstrated that BC and MC differ fundamentally in crystallographic organization. The BC diffractogram contains cellulose-I-associated reflections at 2θ = 14.65° and 22.85°, corresponding to d-spacings of approximately 6.04 Å and 3.89 Å, respectively [36]. These reflections are consistent with ordered cellulose-I domains. Using the conventional cellulose *I* Segal method, the BC crystallinity index was calculated, finding the maximum intensity in the (200) crystalline region (~22–23°) and the minimum intensity associated with the amorphous contribution in the ~18–20° region [37]. This high crystallinity index further corroborates the FTIR findings; since residual bacterial biomass and culture medium byproducts are predominantly amorphous, their presence would otherwise distort the scattering background [32]. Apparent coherent-domain sizes and d-spacings were calculated using standard mathematical frameworks from baseline-corrected intensities [38], while for BC, crystallite size was estimated from the defined crystalline reflection using the Scherrer equation [39]. No Scherrer crystallite size was calculated for MC because its diffraction profile was dominated by broad amorphous scattering. In comparison, MC displayed broad scattering maxima near 8.71° and 19.85°, consistent with a predominantly amorphous structure. These features were not assigned to defined crystallographic planes, and no Scherrer crystallite size was calculated for MC [35].

3.4. Hydrogel Ink Characterization

The four hydrogel formulations were balanced as a 2 × 2 factorial screening matrix, to match the exploratory nature of this proof-of-concept study. To build a dependable benchmark, it was paired to a well-known commercial reference—semi-amorphous MC in Formulations 1 and 2—against a sustainable alternative containing the highly crystalline BC nanofibrils in Formulations 3 and 4. At the same time, the concentration of the bioactive mineral phase (Si-HA) varied using mass ratios of 1 and 0.5 in both polymer groups. This symmetrical setup gives us a clear, uncluttered view to isolate and understand how fiber morphology and mineral loading together shape the composite matrix.

Table 4 summarizes the reduced viscosity, swelling behavior, and mass loss of the four formulations and allows comparison of both variables included in the screening design: the cellulose component (MC or BC) and the Si-HA loading. Capillary-viscosity measurements were performed on the uncrosslinked precursor formulations, prior to $CaCl_2$-mediated

pre-crosslinking. Reduced viscosity followed the order F2 (15.35 dL/g) > F4 (14.74 dL/g) > F3 (12.85 dL/g) > F1 (8.10 dL/g). At the higher Si-HA ratio (1.0), replacement of MC with BC increased the measured reduced viscosity from 8.10 dL/g in F1 to 12.85 dL/g in F3. At the lower Si-HA ratio (0.5), the values for the MC- and BC-containing formulations were closer, reaching 15.35 dL/g for F2 and 14.74 dL/g for F4. Within both material groups, reducing the Si-HA ratio from 1.0 to 0.5 was associated with an increase in reduced viscosity. Since these measurements were performed at a single dilution, they are interpreted as a comparative capillary-viscosity parameter rather than as a complete rheological characterization of the formulations. These results suggest that mineral loading influenced the hydrodynamic behavior of the diluted formulations, although the present capillary-viscosity measurements do not allow the underlying polymer–mineral interactions to be determined directly.

Table 4. Reduced viscosity, swelling degree, and mass loss of the four composite hydrogel formulations.

Hydrogel Formulation	Reduced Viscosity, [η] (dL/g)	Swelling Degree (%)		Mass Loss (%)		
		24 Hours	48 Hours	1 Day	2 Days	9 Days
F 1 (MC, Si-HA 1.0)	8.10 ± 0.018	81.15 ± 2.56	118.71 ± 2.47	14.63 ± 1.08	14.73 ± 0.58	16.96 ± 0.88
F 2 (MC, Si-HA 0.5)	15.35 ± 0.021	83.85 ± 2.64	127.04 ± 3.13	13.46 ± 0.86	13.80 ± 0.79	15.91 ± 0.93
F 3 (BC, Si-HA 1.0)	12.85 ± 0.022	68.64 ± 3.02	116.61 ± 2.62	14.87 ± 0.93	15.22 ± 0.93	17.06 ± 1.08
F 4 (BC, Si-HA 0.5)	14.74 ± 0.044	77.78 ± 2.87	145.83 ± 2.73	14.55 ± 0.97	14.58 ± 0.75	16.57 ± 0.82

Note: Values are expressed as mean ± SD (n = 4 replicate flow-time measurements for reduced viscosity; n = 3 for swelling and mass-loss assays).

Swelling showed a different formulation-dependent pattern. After 24 h, F1 and F2 exhibited swelling values of 81.15% and 83.85%, respectively, whereas F3 and F4 reached 68.64% and 77.78%. After 48 h, water uptake increased in all formulations. F4 showed the highest swelling value (145.83%), followed by F2 (127.04%), while F1 and F3 reached similar values of 118.71% and 116.61%, respectively. Thus, the results do not indicate a uniform effect of BC on swelling. Instead, the response appears to depend on the combination of cellulose type and Si-HA loading, with the highest long-term water uptake observed for the BC-containing formulation with the lower Si-HA content.

Mass loss followed a similar temporal pattern in all four formulations. After 1 day in PBS, values ranged from 13.46% for F2 to 14.87% for F3 (Table 3) of their initial dry weight [40,41]. This initial 'burst mass loss' is not indicative of polymer backbone cleavage, but rather represents the predictable leaching of uncrosslinked macromolecular fractions (such as highly soluble chondroitin sulfate) and loosely bound surface Si-HA particles during equilibrium swelling. Only limited additional mass loss occurred thereafter, with values of 15.91–17.06% recorded after 9 days. The increase between day 1 and day 9 was therefore relatively small for all formulations: 2.33% for F1, 2.45% for F2, 2.19% for F3, and 2.02% for F4. No clear separation between the MC- and BC-containing groups was observed on the basis of this assay. This flat profile underscores the long-term stability of the ionically crosslinked calcium alginate 'egg-box' core network [42]. Since the present gravimetric assay does not distinguish polymer degradation from component release, the measured values are interpreted as mass loss rather than direct evidence of polymer-chain degradation. Overall, all four formulations retained more than 82% of their initial dry mass after 9 days under the conditions tested. Given the sparse sampling schedule, these data should be interpreted as a preliminary stability assessment rather than as a characterization of degradation kinetics.

The effect of Si-HA loading was evaluated through formulation-dependent changes in reduced viscosity, swelling, and mass loss; no crystallographic analysis of Si-HA within the final composite hydrogels was performed.

For tissue engineering applications, this biphasic degradation behavior—characterized by an immediate mass correction followed by structural stagnation—is highly desirable, as it may ensure the 3D-printed filaments maintain their structural remanence and geometric channels long enough to support cellular colonization and new extracellular matrix synthesis.

3.5. 3D Hydrogel Printing

To bridge the gap between material synthesis and biological validation, a preliminary printing trial was conducted at room temperature, for all hydrogel formulations, to obtain acellular grid-like 3D-printed constructs (Figure 4).

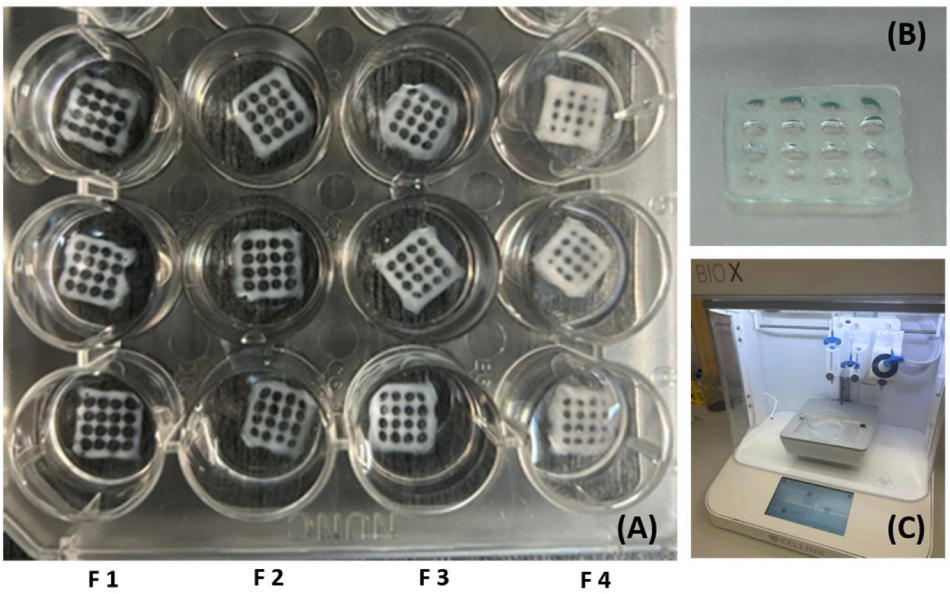


Figure 4. Acellular extrusion printing of MC- and BC-containing hydrogel formulations. (**A**) Representative post-crosslinked grid-like constructs showing open macroporous regions with predominantly rounded pore contours; (**B**) pre-crosslinked 3D construct; (**C**) Bio X extrusion-based 3D printer (Cellink, Brighton, UK) used for hydrogel ink deposition.

Visual inspection showed that all four formulations could be extruded into continuous two-layer grid-like constructs with open and identifiable macroporous regions after crosslinking. The pore openings displayed predominantly rounded to approximately circular contours after printing and crosslinking. As this preliminary study focused on extrusion feasibility, pore geometry was assessed qualitatively and was not used as a quantitative measure of printing fidelity.

3.6. In Vitro Cytocompatibility Testing of Printed Constructs

The cytocompatibility of the acellular 3D-printed constructs was evaluated separately after printing and crosslinking, and the results are presented in Figure 5. All formulations maintained cell viability above the 70% threshold defined by ISO 10993-5 and were therefore classified as non-cytotoxic under the conditions tested [27], thereby confirming the inherent biocompatibility of the crosslinked 3D printed composites.

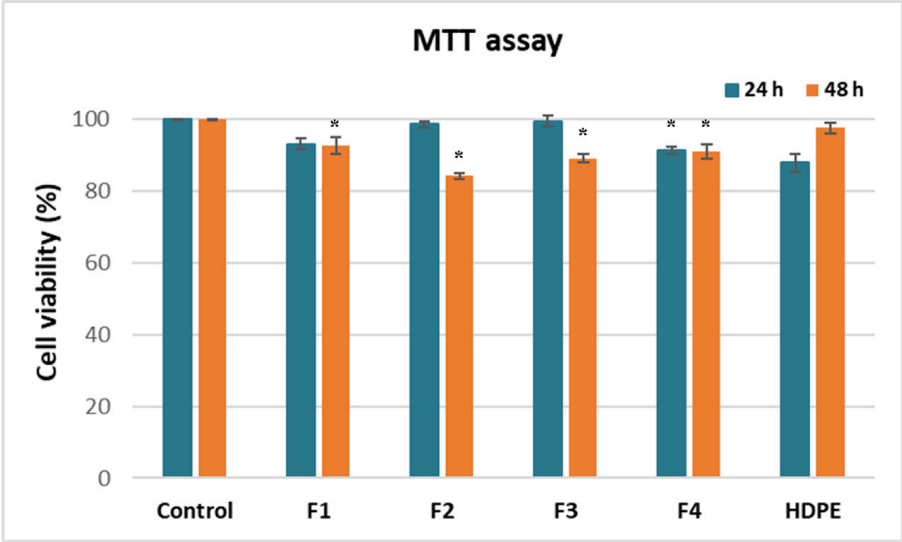


Figure 5. In vitro cytocompatibility of the acellular 3D-printed formulations F1–F4 evaluated by the MTT assay in L929 fibroblasts after 24 and 48 h of direct-contact incubation. Cell viability was normalized to the untreated control (100%). Data are presented as mean ± SD ($n = 3$). Statistical comparisons of F1–F4 against the normalized control value were performed using a one-sample *t*-test with Holm correction for multiple comparisons at each timepoint. * $p < 0.05$. HDPE served as the negative control.

Formulation 2 and 3 yielded the most prominent metabolic response after 24 h, maintaining cell viability similar to untreated cells (control, 100%). This performance underscores the non-toxic and biomimetic surface characteristics introduced by BC nanofibrils when blended with the Si-HA mineral phase. Similarly, Formulation 1 and 4 demonstrated a stable biocompatibility profile, supporting fibroblast viabilities of 93.20% and 91.4%, respectively, at 24 h of cultivation. While the data revealed a minor time-dependent variation in metabolic activity, cell survival was never significantly compromised, maintaining values over 84% at 48 h of cultivation and therefore above the 70% threshold used for non-cytotoxicity assessment according to ISO 10993-5. These results support the short-term cytocompatibility of the four printed formulations and justify further evaluation in more advanced cell-based models, suitable for future 3D bioprinting tissue engineering applications.

3.7. Scanning Electron Microscopy (SEM)

SEM examination provided complementary information on scaffold morphology and cell distribution within the printed structures (Figure 6). The unseeded scaffold controls (Figure 6a–c) show the printed hydrogel architecture at different magnifications. At lower magnification, the grid-like organization and macroporous openings are clearly visible, whereas the higher-magnification images show the continuous but heterogeneous surface of the crosslinked hydrogel matrix.

Constructs after direct-contact incubation with L929 fibroblasts are shown in Figure 6d–j. Panels d–g correspond to formulations F1, F2, F3, and F4, respectively. In all four formulations, fibroblasts were observed mainly as rounded multicellular aggregates adhered on the scaffold surface. The overall morphology of these aggregates was comparable among F1–F4, and no clear formulation-dependent difference could be established from the qualitative SEM observations alone. This spheroidal architecture is typical for hydrophilic polymer networks that lack RGD-mediated cell-adhesive peptides, as cell-to-cell homophilic interactions become thermodynamically favored over cell–substrate spreading.

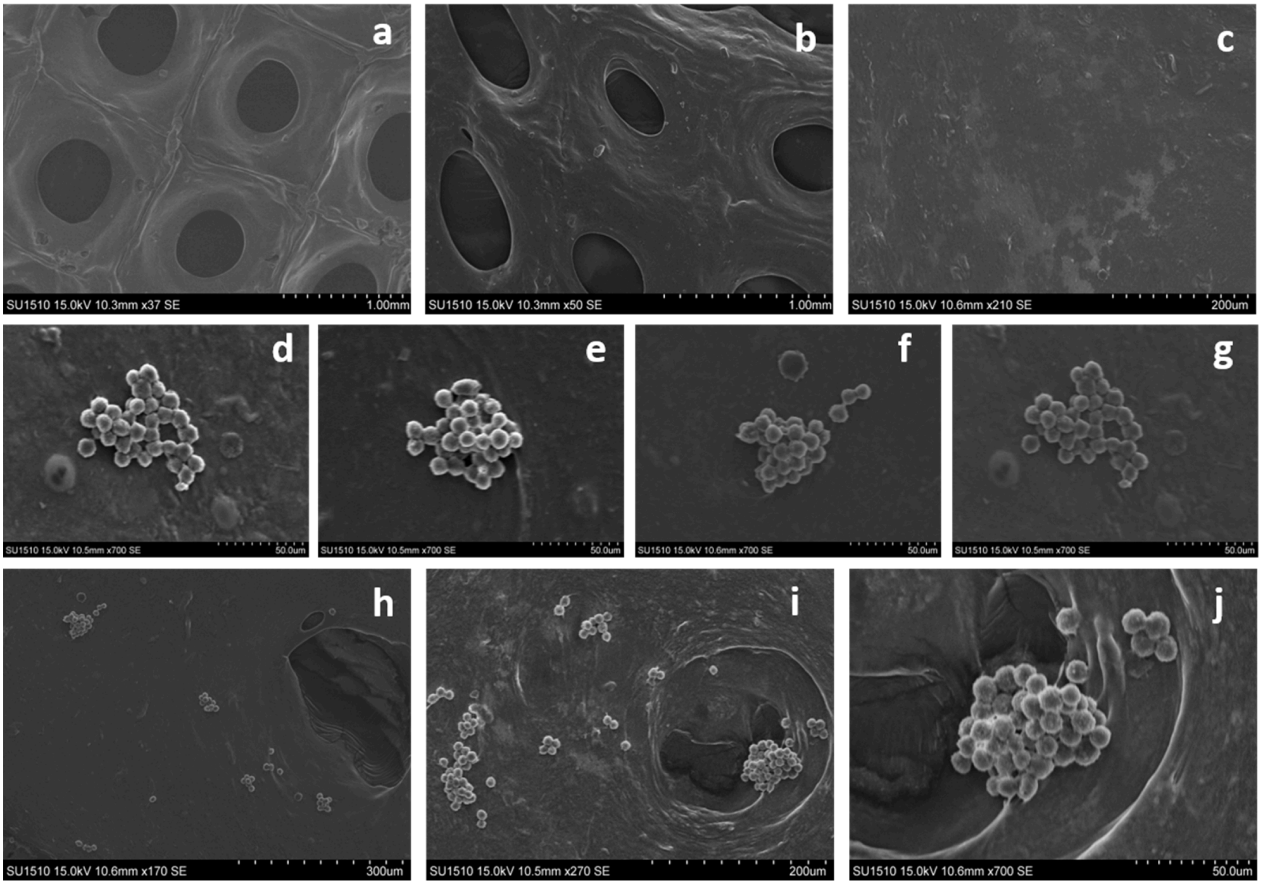


Figure 6. Representative SEM micrographs of the acellular 3D-printed composite hydrogel scaffolds before and after direct-contact incubation with L929 fibroblasts: (**a**–**c**) unseeded scaffold controls, at different magnifications, revealing the printed macrostructural grid filaments and open mesh pores; (**d**–**g**) representative fibroblast aggregates observed on formulations F1, F2, F3, and F4, respectively; (**h**,**i**) lower- and intermediate-magnification views showing the spatial distribution of cellular aggregates in relation to the printed pore openings; and (**j**) higher-magnification detail of a multicellular aggregate located at a pore boundary.

Panels h–j provide additional information on the spatial distribution of the cells within the printed architecture. At lower and intermediate magnification (Figure 6h,i), several cellular aggregates were located close to pore boundaries and within the regions surrounding the printed openings. Figure 6j provides a higher-magnification view of an aggregate positioned at a pore boundary. This suggests that these macroporous openings act as protective architectural anchors that physically trap cell clusters, fostering localized cellular interactions and supporting micro-tissue development.

Compared with the unseeded controls in Figure 6a–c, the cell-seeded samples therefore confirm the presence of fibroblast aggregates on the scaffold surface and indicate that the printed pore geometry may influence their local distribution. These morphological observations visually validate the MTT results but do not provide a quantitative comparison of cell adhesion between formulations.

4. Discussion

This proof-of-concept study evaluated whether physically processed kombucha-derived BC can be incorporated as a nanofibrillar component in alginate/CS/Si-HA composite inks without chemical modification. The results show that BC-containing formulations remained compatible with acellular extrusion printing and short-term cytocompatibility testing under the conditions used.

SEM analysis showed that purified BC formed a highly entangled nanofibrillar network with an average fiber diameter of approximately 86 nm. This morphology provides a large interfacial area that may favor physical entanglement and interactions with the surrounding polymer matrix. FTIR and XRD analyses further highlighted major differences between BC and MC. BC retained strong hydroxyl-associated interactions and a high crystallinity index (85.4%), consistent with preserved cellulose *I* domains, whereas MC displayed a predominantly amorphous structure due to methyl substitution. These structural differences support the proposed role of BC as a nanofibrous component within the hydrogel matrix, rather than solely as a viscosity-modifying phase. The observed nanofibrillar morphology and high crystallinity are consistent with previous reports on microbial BC, where cellulose *I* domains were associated with improved mechanical reinforcement and scaffold stability [30]. XRD characterization was limited to the individual cellulose components, and the crystalline phase of Si-HA within the final composite hydrogels was not assessed. Future studies should include XRD of the complete formulations to evaluate possible changes in mineral phase integrity and matrix–mineral organization after incorporation and crosslinking.

Reduced-viscosity measurements performed on the uncrosslinked precursor formulations indicated that lower Si-HA loading improved polymer hydration and chain mobility in both MC- and BC-based systems. F2 and F4 showed the highest reduced-viscosity values, indicating that Si-HA loading influenced the flow behavior of the precursor formulations under the measurement conditions. Similar effects of mineral loading on polymer mobility were previously reported in alginate-based composite hydrogels, where excessive inorganic content reduced chain flexibility and flow behavior [10].

Swelling and mass-loss behavior depended on both cellulose type and Si-HA loading rather than showing a uniform BC-related trend. At 48 h, F4 exhibited the highest swelling degree (145.83%), whereas F3 remained comparable to the MC-containing formulations. All four formulations showed a similar mass-loss pattern, with most of the measured change occurring during the first 24 h and only limited additional mass loss up to day 9.

All formulations were successfully extruded through a 25 G nozzle, producing grid-like constructs with continuous filaments and preserved pore geometry, although the resulting pore openings displayed rounded rather than ideal square contours. This indicates that both MC- and BC-based formulations exhibited processing behavior compatible with layer-by-layer extrusion under the conditions tested. Notably, BC-based formulations, maintained printability without requiring chemical functionalization. Unlike many reported BC bioinks that require TEMPO oxidation or surface grafting to achieve printable rheology, the current system maintained extrusion capability using only physical BC processing [13,16].

Cytocompatibility testing confirmed non-cytotoxic behavior for all formulations, with cell viability remaining above 84% after 24 and 48 h. SEM observations showed comparable multicellular aggregate morphology across the four formulations, without an evident formulation-dependent pattern. Comparison with the unseeded controls confirmed that the aggregates were associated with the scaffold surface, while the lower-magnification images showed several aggregates close to pore boundaries and printed openings. This distribution suggests that scaffold geometry may influence the local organization of the cells.

Due to its demonstrative nature, this study has several limitations, including the use of BC obtained from a single purification batch, the absence of detailed rheological and mechanical characterization, the qualitative assessment of printing accuracy, limited mass-loss assessment and the use of short-term fibroblast testing only. Quantitative morphometric analysis of filament width, pore dimensions, spreading ratio, and printability index, together with complete rheological characterization of the undiluted inks, including

flow curves and oscillatory measurements of G′ and G″, and evaluation using independent BC batches and more advanced cell-based models, should be included in future studies that will be required in subsequent formulation optimization.

5. Conclusions

This proof-of-concept study showed that physically processed kombucha-derived bacterial cellulose can be incorporated into alginate/CS/Si-HA composite inks without chemical functionalization. Structural characterization confirmed the preservation of the nanofibrillar cellulose-I organization, with a crystallinity index of 85.4%. The formulation study further showed that Si-HA loading influenced reduced viscosity and swelling behavior, while all four formulations exhibited a similar mass-loss pattern, with a similar pattern over the 9-day observation period.

All formulations could be processed by acellular extrusion-based 3D printing through a 25G nozzle into grid-like constructs that retained identifiable macroporous features after ionic crosslinking. Direct-contact testing with L929 fibroblasts showed cell viability above 84% for all formulations, supporting their classification as non-cytotoxic under the conditions tested.

Taken together, these results support the feasibility of using physically processed kombucha-derived BC as a component of alginate-based composite inks. Further work should include rheological, mechanical, and thermal characterization, quantitative assessment of printing fidelity, and evaluation in cell-laden and tissue-specific models.

Author Contributions: Conceptualization, E.U., E.I.O. and O.C.; methodology, E.U., R.T., V.-S.M., D.N.B., M.R. and C.U.; validation, E.U., R.T., V.-S.M., D.N.B., M.R. and C.U.; formal analysis, E.U., R.T., V.-S.M., D.N.B., M.R. and C.U.; investigation, E.U., R.T., V.-S.M., D.N.B., M.R. and C.U.; data curation, E.U., R.T., V.-S.M., E.I.O., D.N.B., M.R. and C.U.; writing—original draft preparation, E.U., R.T., V.-S.M., E.I.O., D.N.B., M.R., C.U. and O.C.; writing—review and editing, E.U., E.I.O. and O.C.; funding acquisition, O.C. All authors have read and agreed to the published version of the manuscript.

Funding: This research was funded by the National Authority of Research, Core Program, project no. 23020201.

Data Availability Statement: The original contributions presented in this study are included in the article. Further inquiries can be directed to the corresponding author.

Acknowledgments: During the preparation of this manuscript, the author(s) used [Gemini 3] for superficial text editing (e.g., grammar, spelling, punctuation, and formatting). The authors have reviewed and edited the output and take full responsibility for the content of this publication.

Conflicts of Interest: The authors declare no conflicts of interest.

References

1. Gouripriya, D.A.; Adhikari, J.; Saha, P. 3D printing of bacterial cellulose for potential wound healing applications: Current trends and prospects. *Int. J. Biol. Macromol.* **2024**, *279*, 135213. [CrossRef] [PubMed]
2. Yu, C.; Zhu, W.; Chen, S.C. Modulating physical, chemical, and biological properties in 3D printing for tissue engineering applications. *Appl. Phys. Rev.* **2018**, *5*, 041101. [CrossRef] [PubMed]
3. Vrana, N.E.; Gupta, S.; Bit, A. From 3D printing to 3D bioprinting: The material properties of polymeric material and its derived bioink for achieving tissue-specific architectures. *Cell Tissue Bank.* **2022**, *23*, 417–440. [CrossRef] [PubMed]
4. Osazee, F.O.; Ohifuemen, A.O.; Otabor, G. Bioink formulations for 3D printing of tissue scaffolds: A review of materials and printability. In Proceedings of the TMS 2024 153rd Annual Meeting & Exhibition Supplemental Proceedings, Orlando, FL, USA, 3–7 March 2024; pp. 484–499.
5. Porwal, S.; Sridhar, S.B.; Malviya, R. 3D printable sustainable hydrogel formulations for tissue engineering applications. *J. Drug Deliv. Sci. Technol.* **2024**, *101*, 106308. [CrossRef]

6. Shavandi, A.; Hamidi, M.; Delattre, C. Biomaterial ink based on bacterial polyglucuronic acid for tissue engineering applications. *Next Mater.* **2024**, *4*, 100181. [CrossRef]
7. Utoiu, E.; Manoi, V.S.; Craciunescu, O. Bacterial cellulose: A sustainable source for hydrogels and 3D-printed scaffolds for tissue engineering. *Gels* **2024**, *10*, 387. [CrossRef] [PubMed]
8. Pillai, M.M.; Tran, H.N.; Bhattacharyya, A. Symbiotic culture of nanocellulose pellicle: A potential matrix for 3D bioprinting. *Mater. Sci. Eng. C* **2021**, *119*, 111552. [CrossRef] [PubMed]
9. Wu, Y.D.; Wang, Y.F.; He, J.M. Preparation of 3D printed polylactic acid/bacterial cellulose composite scaffold for tissue engineering applications. *Polymers* **2022**, *14*, 4756. [CrossRef] [PubMed]
10. Wei, J.X.; Wang, B.X.; Chen, S.Y. A 3D-printable TEMPO-oxidized bacterial cellulose/alginate hydrogel with enhanced stability via nanoclay incorporation. *Carbohydr. Polym.* **2020**, *238*, 116207. [CrossRef] [PubMed]
11. Zielinski, P.S.; Gudeti, P.K.R.; Wlodarczyk-Biegun, M.K. 3D printing of bio-instructive materials: Toward directing the cell. *Bioact. Mater.* **2023**, *19*, 292–327. [CrossRef] [PubMed]
12. Vazquez-Rivas, E.; Desales-Guzman, L.A.; Burillo-Amezcua, S.G. Cellulose-based hybrid hydrogels for tissue engineering applications: A sustainable approach. *Gels* **2025**, *11*, 438. [CrossRef] [PubMed]
13. Hospodiuk-Karwowski, M.; Bokhari, S.M.Q.; Catchmark, J.M. Dual-charge bacterial cellulose as a potential 3D printable material for soft tissue engineering. *Compos. Part B Eng.* **2022**, *231*, 109598. [CrossRef]
14. Lee, S.J.; Lee, J.H.; Park, S.A. Fabrication of 3D printing scaffold with porcine skin decellularized bio-ink for soft tissue engineering. *Materials* **2020**, *13*, 3522. [CrossRef] [PubMed]
15. Baykara, D.; Yilmaz, O.; Gunduz, O. Engineering of a novel SilkMA-bacterial cellulose hydrogel bioink for digital light processing three-dimensional bioprinting. *MRS Bull.* **2026**, *51*, 117–127. [CrossRef]
16. Wang, X.C.; Zhang, Y.B.; Huang, C.X. Printability of hybridized composite from maleic acid-treated bacterial cellulose with gelatin for bone tissue regeneration. *Adv. Compos. Hybrid Mater.* **2023**, *6*, 711–727. [CrossRef]
17. Wang, X.C.; Wu, D.X.; Huang, C.X. Constructing osteo-inductive bio-ink for 3D printing through hybridization of gelatin with maleic acid-modified bacterial cellulose. *J. Bioresour. Bioprod.* **2024**, *9*, 336–350. [CrossRef]
18. Li, H.H.; Chen, S.S.; Wang, M. Gelatin methacryloyl/sodium alginate/cellulose nanocrystal inks and 3D printing for dental tissue engineering applications. *ACS Omega* **2024**, *9*, 48361–48373. [CrossRef] [PubMed]
19. Iglesias-Mejuto, A.; Raptopoulos, G.; Paraskevopoulou, P. 3D-printed cellulose aerogels minimally cross-linked with polyurea: A robust strategy for tissue engineering. *ACS Appl. Mater. Interfaces* **2025**, *17*, 34444–34457. [CrossRef] [PubMed]
20. Cakmak, A.M.; Unal, S.; Kalaskar, D.M. 3D printed polycaprolactone/gelatin/bacterial cellulose/hydroxyapatite composite scaffold for bone tissue engineering. *Polymers* **2020**, *12*, 1962. [CrossRef] [PubMed]
21. Zhao, Q.; Yang, D.F.; Liu, Z.H. Carbon nanotube bacterial cellulose polycaprolactone scaffolds for bone tissue engineering using top-heating fused deposition three-dimensional printing. *Int. J. Biol. Macromol.* **2025**, *318*, 144588. [CrossRef] [PubMed]
22. Jia, W.D.; Liu, Z.X.; Sang, S.B. 3D bioprinting-based dopamine-coupled flexible material for nasal cartilage repair. *Aesthetic Plast. Surg.* 2024, *in press*. [CrossRef] [PubMed]
23. Utoiu, E.; Matei, F.; Toma, A.; Diguță, C.F.; Ștefan, L.M.; Mănoiu, S.; Vrăjmașu, V.V.; Moraru, I.; Oancea, A.; Israel-Roming, F.; et al. Bee collected pollen with enhanced health benefits, produced by fermentation with a Kombucha consortium. *Nutrients* **2018**, *10*, 1365. [CrossRef] [PubMed]
24. Gu, L.; Li, T.; Song, X.; Yang, X.; Li, S.; Chen, L.; Liu, P.; Gong, X.; Chen, C.; Sun, L. Preparation and characterization of methacrylated gelatin/bacterial cellulose composite hydrogels for cartilage tissue engineering. *Regen. Biomater.* **2020**, *7*, 195–202. [CrossRef] [PubMed]
25. Gaspar-Pintiliescu, A.; Seciu, A.M.; Miculescu, F.; Moldovan, L.; Ganea, E.; Craciunescu, O. Enhanced extracellular matrix synthesis using collagen dressings loaded with Artemisia absinthium plant extract. *J. Bioact. Compat. Polym.* **2018**, *33*, 516–528. [CrossRef]
26. Fatma, Z.K.; Muhammad, Y.; Ihtesham, U.R. In vitro degradation, swelling, and bioactivity performances of in situ forming injectable chitosan-matrixed hydrogels for bone regeneration and drug delivery. *Biotechnol. Bioeng.* **2024**, *121*, 2767–2779. [CrossRef] [PubMed]
27. *ISO 10993-5*; Biological Evaluation of Medical Devices—Part 5: Tests for In Vitro Cytotoxicity, 3rd ed. International Organization for Standardization: Vernier, Switzerland, 2009.
28. Stefan, L.M.; Iosageanu, A.; Ilie, D.; Stanciuc, A.-M.; Matei, C.; Berger, D.; Craciunescu, O. Extracellular matrix biomimetic polymeric membranes enriched with silver nanoparticles for wound healing. *Biomed. Mater.* **2021**, *16*, 035010. [CrossRef] [PubMed]
29. Utoiu, E.; Plangu, A.; Manoiu, V.-S.; Oprita, E.I.; Tatia, R.; Utoiu, C.; Craciunescu, O. Kefiran as a novel biomaterial ink component: Preliminary assessment of 3D printing feasibility and biocompatibility. *Gels* **2026**, *12*, 279. [CrossRef] [PubMed]
30. Reiniati, I.; Hrymak, A.N.; Margaritis, A. Recent developments in the production and applications of bacterial cellulose fibers and nanocrystals. *J. Appl. Polym. Sci.* **2017**, *134*, 43720.

31. Jorfi, M.; Foster, E.J. Recent advances in nanocellulose for biomedical applications. *J. Appl. Polym. Sci.* **2015**, *132*, 41719. [CrossRef]
32. Grube, M.; Shvirksts, K.; Denina, I.; Ruklisa, M.; Semjonovs, P. Fourier-transform infrared spectroscopic analyses of cellulose from different bacterial cultivations. *Vib. Spectrosc.* **2016**, *84*, 53–57. [CrossRef]
33. Ghozali, M.; Meliana, Y.; Chalid, M. Synthesis and characterization of bacterial cellulose by Acetobacter xylinum using liquid tapioca waste. *Mater. Today Proc.* **2021**, *44*, 2131–2134. [CrossRef]
34. Umamaheswari, S.; Oli, M.; Naveena, K. FTIR spectral and microarchitectural analysis of cellulose produced by Lactococcus lactis under agitated condition. *J. Pure Appl. Microbiol.* **2017**, *11*, 1965–1971. [CrossRef]
35. Ahlfeld, T.; Guduric, V.; Duin, S.; Akkineni, A.R.; Schütz, K.; Kilian, D.; Emmermacher, J.; Cubo-Mateo, N.; Dani, F.; Witzleben, M.V.; et al. Methylcellulose—A versatile printing material that enables biofabrication of tissue equivalents with high shape fidelity. *Biomater. Sci.* **2020**, *8*, 2102–2110. [CrossRef] [PubMed]
36. French, A.D. Idealized powder diffraction patterns for cellulose polymorphs. *Cellulose* **2014**, *21*, 885–896. [CrossRef]
37. Segal, L.; Creely, J.J.; Martin, A.E.; Conrad, C.M. An empirical method for estimating the degree of crystallinity of native cellulose using the X-ray diffractometer. *Text. Res. J.* **1959**, *29*, 786–794. [CrossRef]
38. Cullity, B.D.; Stock, S.R. *Elements of X-Ray Diffraction*, 3rd ed.; Prentice Hall: Upper Saddle River, NJ, USA, 2001; pp. 562–568.
39. Scherrer, P. Bestimmung der Größe und der inneren Struktur von Kolloidteilchen mittels Röntgenstrahlen. *Nachr. Ges. Wiss. Göttingen* **1918**, *2*, 98–100.
40. Huang, X.; Brazel, C.S. On the importance and mechanisms of burst release in matrix-controlled drug delivery systems. *J. Control. Release* **2001**, *73*, 121–136. [CrossRef] [PubMed]
41. Agbna, G.H.D.; Zaidi, S.J. Hydrogel performance in boosting plant resilience to water stress—A review. *Gels* **2025**, *11*, 276. [CrossRef] [PubMed]
42. Cao, L.; Lu, W.; Mata, A.; Nishinari, K.; Fang, Y. Egg-box model-based gelation of alginate and pectin: A review. *Carbohydr. Polym.* **2020**, *242*, 116389. [CrossRef] [PubMed]

Disclaimer/Publisher's Note: The statements, opinions and data contained in all publications are solely those of the individual author(s) and contributor(s) and not of MDPI and/or the editor(s). MDPI and/or the editor(s) disclaim responsibility for any injury to people or property resulting from any ideas, methods, instructions or products referred to in the content.